Rare Metal Materials and Engineering
Volume 54, Issue 9, September 2025
Available online at www.rmme.ac.cn

Science Press

Cite this article as: Guo Jianbo, Liu Zhengjun, Su Yunhai. Influence of Y Content on Formability and Wear Properties of Fe-Cr-C-B-Ti Cladding Metals[J]. Rare Metal Materials and Engineering, 2025, 54(09): 2256-2264. DOI: https://doi.org/10.12442/j.issn.1002-185X.20240458.

ARTICLE

Influence of Y Content on Formability and Wear Properties of Fe-Cr-C-B-Ti Cladding Metals

Guo Jianbo, Liu Zhengjun, Su Yunhai

School of Materials Science and Engineering, Shenyang University of Technology, Shenyang 110870, China

Abstract: The failure of mechanical components is mainly caused by three key mechanisms: wear, corrosion, and fatigue. Among these failure modes, wear of mechanical components notably increases energy consumption and leads to substantial economic losses. Fe-Cr-C-B-Ti-Y wear-resistant cladding metals were prepared by the plasma cladding method. The wear performance of the cladding metals was analyzed using an MLS-23 rubber wheel wet sand wear tester. X-ray diffraction, scanning electron microscope, electron backscatter diffraction, and transmission electron microscope were employed to investigate the phase composition and microstructure of the cladding metals, followed by a discussion of their strengthening and wear mechanisms. The results indicate that the microstructure of Fe-Cr-C-B-Ti-Y cladding metals is composed of austenite γ-Fe, M_{23}(C,B)$_6$ eutectic carbide, and TiC hard phase. As the Y_2O_3 content increases, the hardness and wear resistance of the cladding metal show a trend of first increasing and then decreasing. When the Y_2O_3 content is 0.4wt%, the precipitation of TiC hard phase and M_{23}(C, B)$_6$-type eutectic carbides reaches maximum, and the grain size is the finest. The cladding metal exhibits optimal formability, featuring the smallest wetting angle of 52.2°. Under this condition, the Rockwell hardness value of the cladding metal is 89.7 HRC, and the wear mass loss is 0.27 g. The dominant wear mechanism of cladding metals is abrasive wear, and the material removal process involves micro-cutting and plowing.

Key words: Fe-Cr-C-B; cladding metal; nano-Y_2O_3; ceramic phase; wear resistance

1 Introduction

With the rapid development of science and technology, the performance requirements for materials applied in tool manufacturing and mechanical engineering are gradually increasing. In practical service, the failure of mechanical parts, tools, and molds predominantly stems from material fatigue or wear rather than brittle fracture. Fe-Cr-C surfacing alloy is a widely adopted category of wear-resistant materials, where the hard phases such as MC, M_7C_3, and $M_{23}C_6$ are uniformly dispersed within the matrix to enhance abrasion resistance[1–2].

The wear resistance of Fe-based hardfacing alloys arises from the synergistic effect between the carbide hard phase with high-hardness and the matrix with strong toughness. Feldshtein et al[3] designed an Fe-Cr-W-C powder and successfully prepared an iron-based alloy cladding layer. Their study found that the coating consisted of fine primary austenite dendrites and an austenite-M_7C_3 eutectic structure, with a Vickers microhardness reaching up to 8 GPa. Debta et al[4] deposited a TiC-Co-$n$$Y_2O_3$ cladding layer on Ti-6Al-4V alloy plate by tungsten inert gas (TIG) cladding method. With the addition of nano-Y_2O_3, the melting efficiency of TIG welding was improved, and the TiC particles were completely melted, which transformed into slender dendrites during the solidification process. This modification endowed the alloy with excellent mechanical properties: the average microhardness increased slightly, while the friction coefficient decreased significantly. Compared with TiC-Co deposited metal, the wear of TiC-Co-2%Y_2O_3 coating was reduced by nearly fourfold. The addition of nano-Y_2O_3 effectively purified grain boundaries, refined the grain structure, and enhanced the fracture toughness of the deposited metal. During sliding wear testing, the brittle cracking and extraction of TiC particles were suppressed, and the absolute wear resistance of the coating was improved. Shi et al[5] added Y_2O_3

Received date: August 25, 2024

Corresponding author: Su Yunhai, Ph. D., Professor, School of Materials Science and Engineering, Shenyang University of Technology, Shenyang 110870, P. R. China, E-mail: 289646841@qq.com

to an Fe-Cr-C-Nb surfacing alloy and found that Y_2O_3 can act as a heterogeneous nucleation core for *M*C, refining the hard phase *M*C and promoting its uniform distribution. Concurrently, the wear resistance of the deposited alloy has been improved.

Rare earth elements are a series of metal elements with similar physical and chemical properties. Owing to their unique electronic structures, strong chemical reactivity, and large ion radii, they play an important role in grain refinement during metal cladding[6]. Introducing rare earth elements appropriately into cladding metals can effectively promote grain refinement, reduce crack tendency, and comprehensively improve the hardness, corrosion resistance, and wear resistance of the surface layer of cladding metals[7–9]. The addition of nano-Y_2O_3 to cladding metals can serve as heterogeneous nucleation sites for the secondary refinement of $M_{23}C_6$ eutectic carbides in hard phases. In this research, Fe-Cr-C-B-Ti-Y wear-resistant cladding metals prepared by plasma cladding, and the effects of rare earth oxide Y_2O_3 (0wt% – 0.5wt%) on the microstructure and wear resistance of Fe-Cr-C-B-Ti cladding metals were investigated.

2 Experiment

2.1 Preparation of cladding metals

Q235 carbon structural steel was selected as the substrate material, and its chemical composition is listed in Table 1. Prior to cladding, the substrate surface was cleaned using an angle grinder for comprehensive rust removal and polishing. This procedure ensured the complete removal of rust, impurities, and oxide film, yielding a clean surface for subsequent operations.

Table 1 Chemical composition of Q235 (wt%)

C	Si	Mn	P	S
0.12–0.20	<0.30	0.30–0.70	–0.045	–0.045

The main components of the composite strengthening alloy include chromium nitride (61.5% Cr, 18% N), chromium powder (99% Cr), boron iron powder (18% B), high-silicon iron powder (75% Si), reduced iron powder, titanium powder (99% Ti), etc. The particle size of alloy powder was 150 – 178 μm. The designed composition was Fe-25Cr-5C-2B-6Ti-Y (0wt% – 0.5wt%) cladding alloy. The alloy powders were uniformly mixed and stirred to ensure even distribution of each element in the strengthened alloy system. The particles were ground evenly and finely using a ball mill. Since the metal powder is highly hygroscopic and damp flux-cored welding wires are prone to defects such as pores and cracks[10], the powder should be dried in advance. Fig. 1 shows the scanning electron microscope (SEM) images of the base powders and the schematic diagram of plasma welding. The prepared alloy powder was deposited onto the surface of Q235 steel plate using a plasma welding machine to prepare the corresponding cladding metals. The cladding process parameters are shown in Table 2.

2.2 Microstructure and performance testing

After mechanical processing of the cladding layer, X-ray

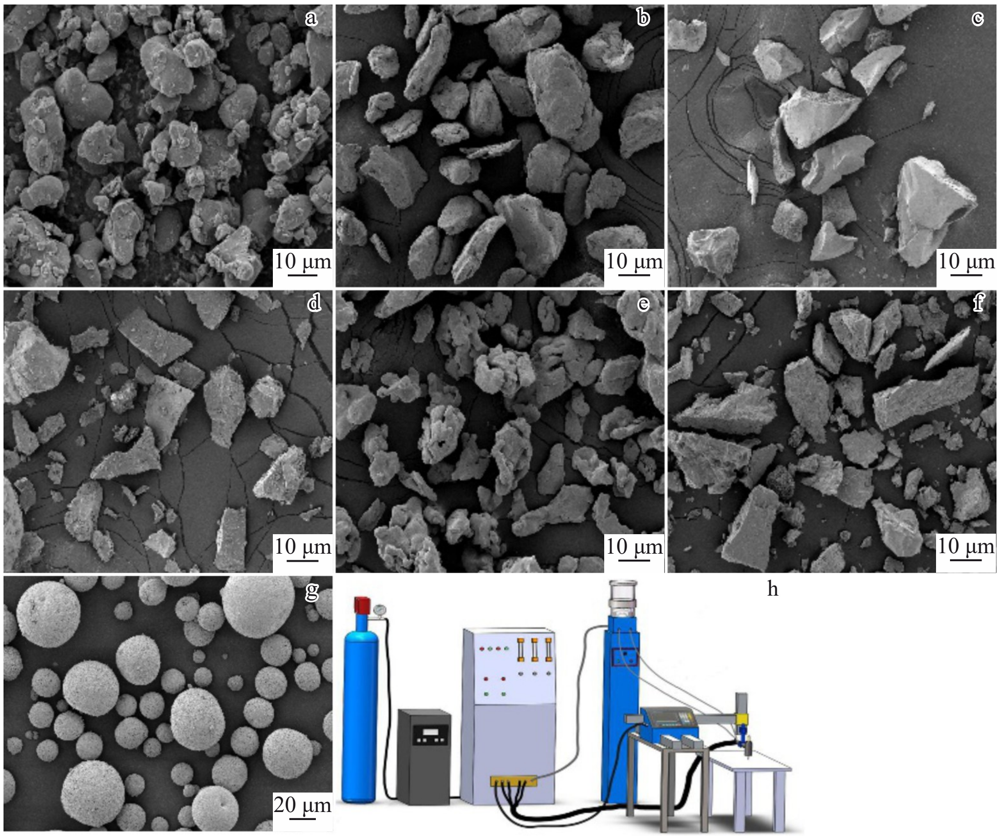

Fig.1 SEM images of mixed powder (a–g) and schematic of plasma welding (h)

Table 2 Welding process parameters

Arc voltage/V	Welding current/A	Welding speed/ $m\cdot h^{-1}$	Gas flow rate/ $L\cdot min^{-1}$
32	190	10	20

diffractometer (XRD) was employed to characterize its phase structure using a pure Cu target, operating at 40 kV tube voltage and 30 mA tube current. The scanning parameters were set as a step size of 2°/min over a range of 0°–100°. The microstructure, phase distribution, and worn surface morphology of the cladding layer were observed using the S-3400N SEM, and the specific composition of the precipitated phase was identified using the energy dispersive spectroscope (EDS) equipped into SEM. Electron backscatter diffraction (EBSD) was used to analyze microstructure information such as grain size and volume percentage of precipitates. For in-depth characterization, a FEI TalosF200X transmission electron microscope (TEM) with selected area electron diffraction (SAED) was used to determine the type and structure of precipitates in the cladding metals, and the composition of precipitates was determined using an EDS. The surface hardness measurement of the cladding metals was carried out using the Rockwell hardness tester (HRS-150, Shanghai, China), while cross-sectional microhardness was tested using a Vickers hardness tester (TMVP-1T, Beijing, China) under a load of 1 kg and a dwell time of 15 s. Abrasive wear tests were conducted on an MLS-23 rubber wheel wet sand tester with the following experimental parameters: rubber wheel rotation speed of 240 r/min, quartz sand particle size of 270–830 μm, wear duration of 5 min, and a maximum normal pressure of 23 kg applied to the rubber wheel.

3 Results and Discussion

3.1 Phase structure

Fig. 2 shows the XRD patterns of cladding metals with different Y_2O_3 contents. It is evident that the cladding matrix retains an austenitic structure (γ-Fe), with primary hard phases consisting of $M_{23}(C,B)_6$ eutectic carbides and TiC. Compared to the Y_2O_3-free cladding metals, the diffraction peak intensity of TiC of Y_2O_3-modified cladding metals is more pronounced, because Y_2O_3, as the heterogeneous nucleation cores, can improve the nucleation rate and promote the formation of TiC hard phase. The introduction of Y does not alter the phase composition but predominantly influences the microstructure by refining grains and purifying grain boundaries.

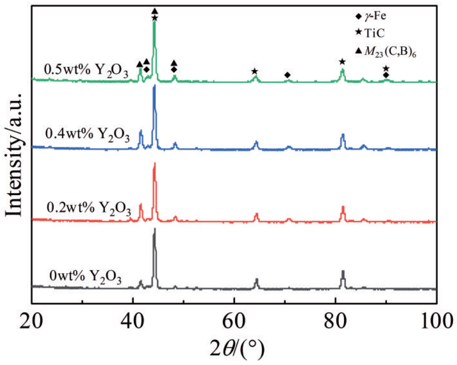

Fig.2 XRD patterns of cladding metals with different Y_2O_3 contents

3.2 Microstructure

Good wettability and small contact angle are necessary conditions to ensure interface bonding. According to the Young Dupre equation[11], Eq.(1) can be inferred.

$$\cos\theta = (\sigma_{sg} - \sigma_{sl})/\sigma_{lg} \quad (1)$$

where θ denotes wetting angles; σ_{sg} is the surface tension at one end of the substrate; σ_{sl} is the interface tension between cladding metals and the substrate; σ_{lg} is the surface tension of the liquid. When the surface tension of the cladding metals is low, the contact angle decreases, leading to improved wettability. That is to say, the wetting effect of the molten metal on the substrate surface can be improved by reducing the surface tension of the molten metal[12].

Incorporating rare earth elements into cladding metals enhances powder flowability and wettability in metal matrix composites, thereby reducing porosity and other defects, and ultimately improving weld bead formation[13]. Fig.3 shows the morphologies of cladding metals with different Y_2O_3 contents. As the Y_2O_3 addition increases from 0wt% to 0.4wt%, the splashing rate of the cladding metals gradually decreases, along with reduced smoke and dust. The formability of the cladding metals is optimal, and wetting angle gradually decreases to 52.2°. When the Y_2O_3 content reaches 0.5wt%, cracks and pores appear on the cladding surface, resulting in

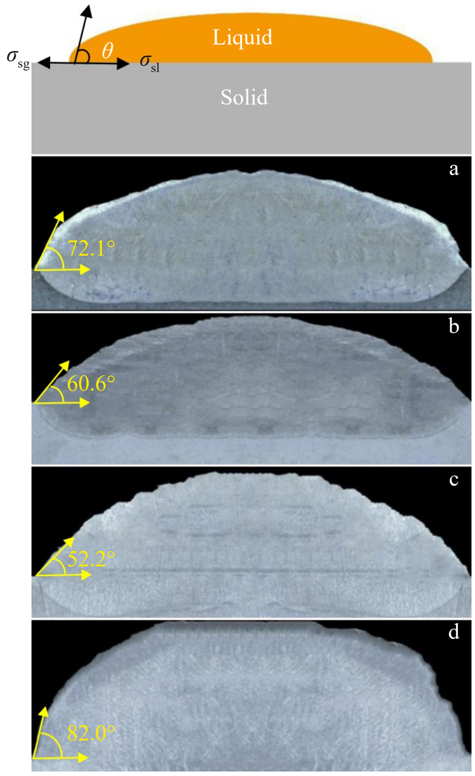

Fig.3 Morphologies of cladding metals with different Y_2O_3 contents: (a) 0wt%, (b) 0.2wt%, (c) 0.4wt%, and (d) 0.5wt%

poor formability and an increase in wetting angle to 82.0°. These results clearly demonstrate that the appropriate addition of Y_2O_3 can promote the formability of cladding metals.

Fig. 4 shows the microstructures of cladding metals with different Y_2O_3 contents. As shown in Table 3, the cladding metals exhibit a typical eutectic structure, where the matrix is composed of austenite γ-Fe, and the precipitated phase consists of network-like eutectic carbides $M_{23}(C,B)_6$ and black block-like TiC precipitates. When the Y_2O_3 addition is 0.4wt%, the grains of the cladding metal are the finest, changing from coarse dendrites to equiaxed grains. Compared with the Y_2O_3-free sample, this addition hinders the migration of grain boundaries and refines the microstructure of the cladding metals. The precipitation of $M_{23}(C, B)_6$ eutectic carbides and TiC hard phases reaches a maximum and they are evenly distributed. This phenomenon is attributed to the incomplete melting characteristics of high-melting-point Y_2O_3 during the welding process: the partially melted Y_2O_3 particles serve as effective heterogeneous nucleation sites in the deposited metal, enhancing nucleation activity and promoting the effective generation of TiC hard phases. A large number of dispersed TiC particles can effectively anchor grain boundaries, suppress their movement, and thus achieve grain refinement[14]. When the Y_2O_3 content increases to 0.5wt%, the structure transforms into coarser dendrites, mainly because excessive Y_2O_3 reduces the melt fluidity, weakens convection, and slows the cooling rate of the melt, providing time for the dendrite growth[15]. This indicates that appropriate Y_2O_3 addition is crucial for refining grain size and enhancing the wear resistance of cladding metals.

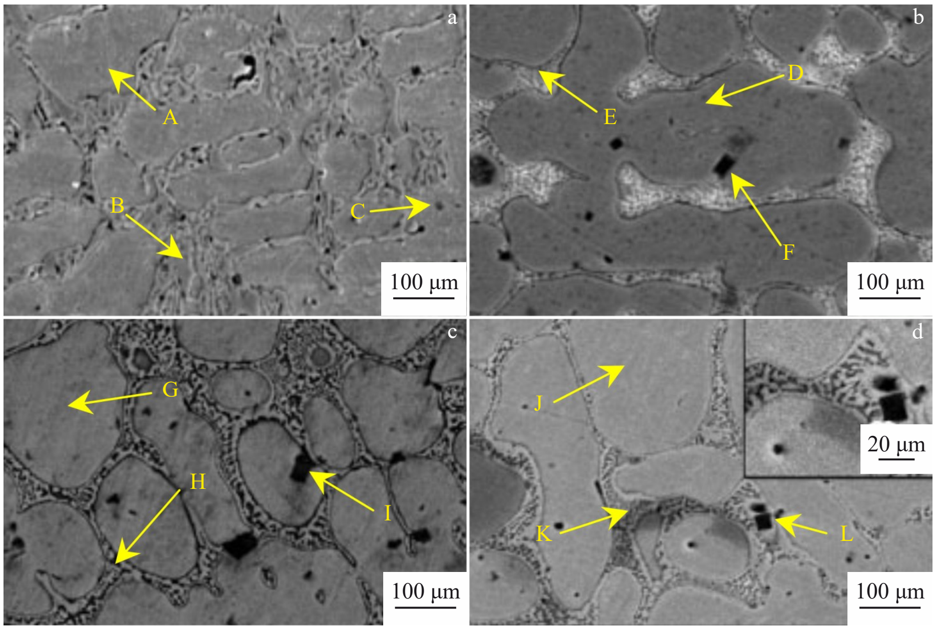

Fig.4 Microstructures of cladding metals with different Y_2O_3 contents: (a) 0wt%, (b) 0.2wt%, (c) 0.4wt%, and (d) 0.5wt%

Table 3 EDS analysis results of points marked in Fig.4 (wt%)

Point	B	C	Ti	Cr	Fe	Y
A	5.40	3.64	0.77	14.68	75.51	-
B	2.87	4.08	0.60	28.27	64.18	-
C	1.94	14.36	50.82	10.54	22.34	-
D	5.28	3.59	0.64	13.76	76.60	0.13
E	2.37	4.22	0.83	27.11	65.20	0.27
F	1.27	14.26	54.63	9.89	19.71	0.24
G	5.98	3.52	0.46	10.53	79.17	0.34
H	5.12	5.34	0.91	22.75	65.47	0.41
I	3.35	15.43	62.89	7.83	10.11	0.39
J	5.03	3.47	0.67	11.68	78.87	0.28
K	5.59	6.14	1.22	22.18	64.40	0.47
L	3.06	14.76	63.29	8.51	9.77	0.61

Fig. 5 shows TEM images of the hard phase in cladding metals with 0.4wt% Y_2O_3. From Fig. 5a, it can be observed that the hard phase exhibits a block-like morphology, with black strip-shaped particles distributed in its internal area. In Fig.5b, region A shows a typical fcc structure, identifying TiC as the hard phase with a crystal band axis of [011]. In Fig.5c, it is calibrated and determined to be Y_2O_3. In Fig.5d, the two phases overlap, indicating that TiC and Y_2O_3 can form heterogeneous nucleation interfaces. In this mechanism, Y_2O_3 acts as an effective nucleation site, not only promoting the generation of TiC, but also refining the grain size and facilitating the precipitation of eutectic carbides. In summary, the addition of Y_2O_3 significantly enhances the wear resistance of the cladding metals.

Fig.6 shows the EBSD inverse pole figures (IPFs) and grain size statistics of cladding metals with different Y_2O_3 contents. When the Y_2O_3 addition increases to 0.4wt%, the grain size of the cladding metal is significantly refined. Specifically, the

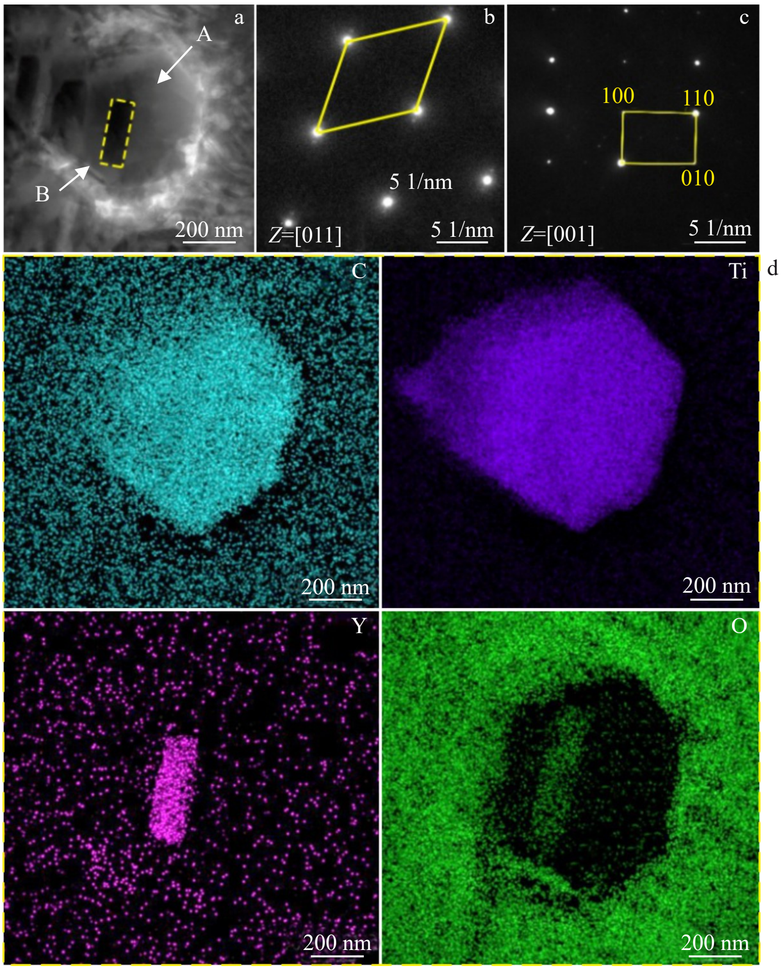

Fig.5 TEM image of TiC (a); SAED patterns of region A (b) and region B (c) marked in Fig.5a; EDS elemental mappings (d)

average grain size decreases from the initial 3.42 μm to 2.35 μm. Meanwhile, the grain size distribution tends to be more uniform. However, when the content of Y_2O_3 is further increased to 0.5wt%, the grain size of the cladding metal shows a reverse change, increasing to 3.87 μm with a non-uniform distribution. The relationship between grain size and yield strength can be described by the Hall-Petch equation[16]:

$$\sigma_s = \sigma_i + kd^{-1/2} \tag{2}$$

where σ_s indicates the yield stress of the material, σ_i represents the lattice resistance encountered by dislocation movement, k is a proportional constant, and d represents the grain size. The formula reveals that the smaller the grain size, the higher the yield stress of the material. Generally, the hardness of a material is positively correlated with strength. Therefore, appropriately adding Y_2O_3 to refine the grain structure of the cladding metals directly contributes to a significant increase in hardness. However, when the Y_2O_3 addition exceeds the appropriate range, the microstructure of the cladding metals will become coarse, and this structural change will lead to a decrease in hardness.

3.3 Hardness

Fig.7 shows a histogram of Rockwell hardness changes for cladding metals with different Y_2O_3 contents. The effect of Y_2O_3 content on the hardness of cladding metals shows a trend of first increasing and then decreasing. The hardness of the Y_2O_3-free cladding metals is 61.0 HRC. When the Y_2O_3 addition is adjusted to 0.4wt%, the Rockwell hardness significantly increases to 89.7 HRC, with a increment of 47%. From the observation of microstructure, it can be concluded that increasing Y_2O_3 content does not significantly affect the volume fraction of matrix austenite in the cladding metals. In contrast, the volume fractions of $M_{23}(C,B)_6$ eutectic carbides and TiC precipitates increase significantly. These high-density $M_{23}(C,B)_6$ eutectic carbides and TiC precipitates are uniformly and finely dispersed in the matrix, which is the reason for the enhanced hardness of the cladding metals. However, when the content of Y_2O_3 further increases to 0.5wt%, the flowability of the molten pool of the cladding metals begins to weaken, hindering the effective discharge of inclusions and gases, thereby leading to defect formation. At the same time, the cooling rate of the molten pool of the cladding metals slows down, prolonging the time for microstructure formation, ultimately resulting in a coarse grain structure of the cladding metals. The combined effect of these factors causes a decrease in hardness of cladding metals[17].

Fig.8 shows the variation of microhardness on the side of the cladding metals with different Y_2O_3 contents. With the increasing Y_2O_3 addition, the microhardness of the cladding

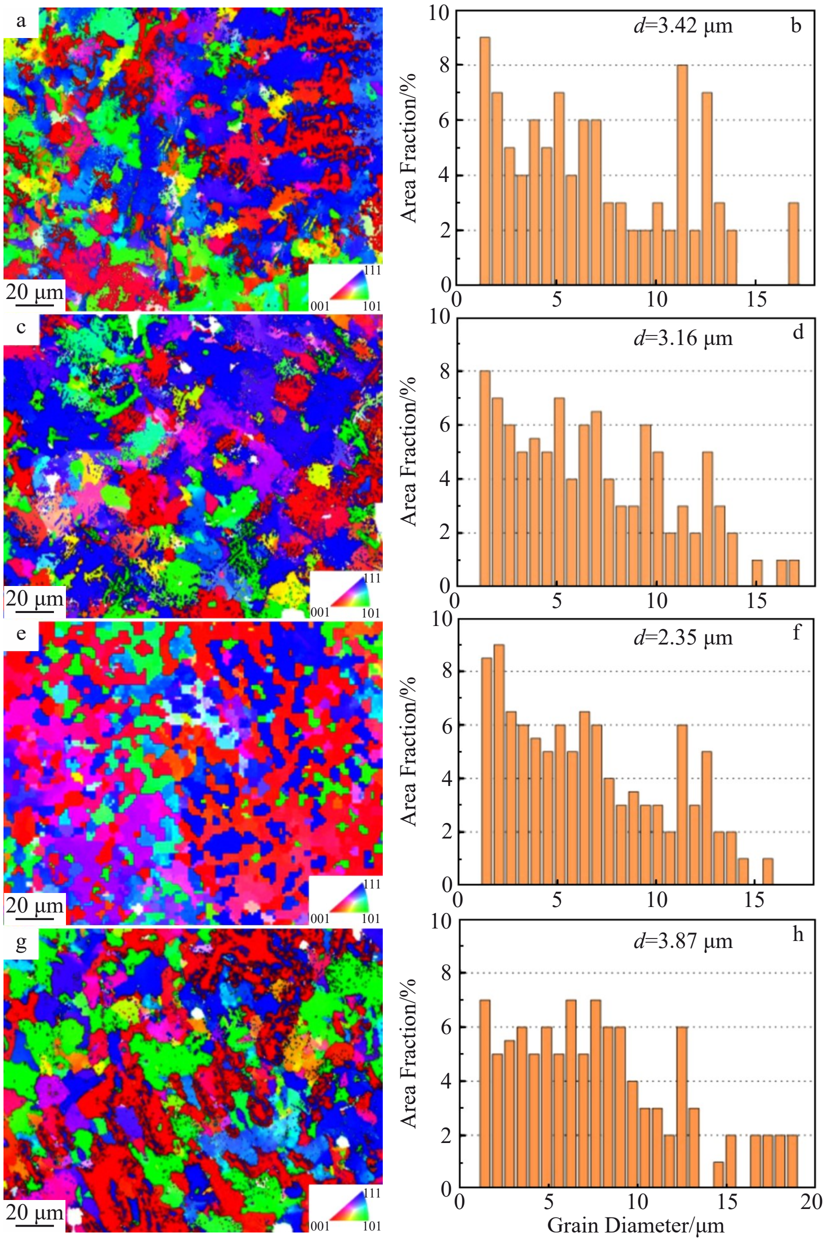

Fig.6 IPFs (a, c, e, g) and grain size statistics (b, d, f, h) of cladding metals with different Y_2O_3 contents: (a–b) 0wt%, (c–d) 0.2wt%, (e–f) 0.4wt%, and (g–h) 0.5wt%

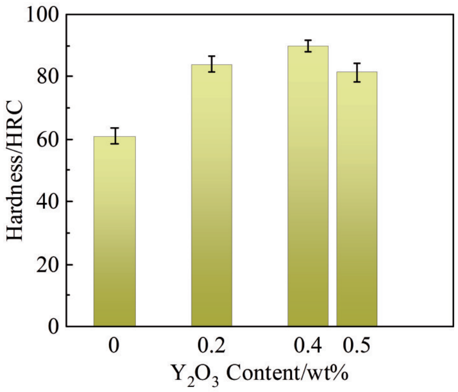

Fig.7 Surface Rockwell hardness of cladding metals with different Y_2O_3 contents

metals undergoes a process of first increasing and then decreasing. When the content of Y_2O_3 reaches 0.4wt% , microhardness of the cladding metals reaches its peak of 1003 HV, increased by 35.7% compared to that of the Y_2O_3-free sample. The microhardness of matrix material Q235 is relatively low, about 270 HV. Near the surface area of the cladding metals, the microhardness gradually increases, mainly due to the dilution effect of the substrate, which reduces the precipitation of $M_{23}(C,B)_6$ eutectic carbides in the cladding metals, thereby suppressing the microhardness enhancement to a certain extent.

3.4 Wear resistance

Fig. 9 shows the changes in wear mass loss of cladding metals with different Y_2O_3 contents. The wear mass loss of the

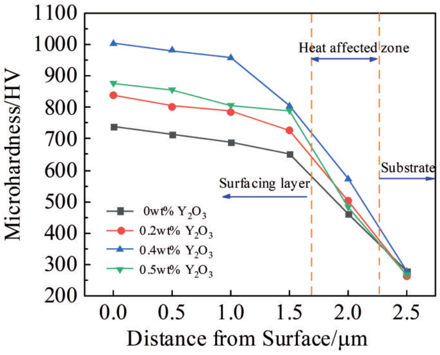

Fig.8 Microhardness on the side of cladding metals with different Y_2O_3 contents

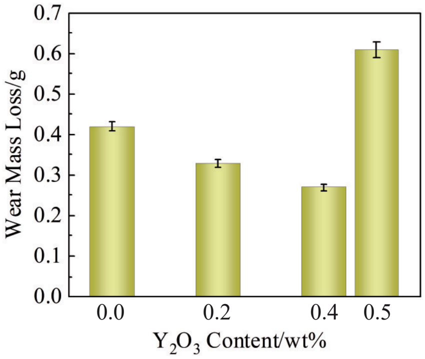

Fig.9 Wear mass loss of cladding metals with different Y_2O_3 contents

cladding metals decreases first and then increases with the increase in Y_2O_3 content. When the Y_2O_3 content reaches 0.4wt%, the wear performance is optimal, with the minimum mass loss of only 0.27 g. Compared with the Y_2O_3-free cladding metals, the wear resistance of Y_2O_3-modified cladding metals is improved by 55.56%. However, as the content Y_2O_3 further increases to 0.5wt%, the wear mass loss significantly increases and the wear resistance deteriorates. The wear resistance of the cladding metals varies with Y_2O_3 addition, which is consistent with the hardness trend. The appropriate addition of Y_2O_3 can promote a richer and more uniform distribution of TiC hard phases, while optimizing the precipitation and distribution of $M_{23}(C,B)_6$ eutectic carbides. The increase in hard phases is directly related to the enhancement of hardness and wear resistance[18]. The austenitic matrix, due to its work hardening characteristics, can form a work-hardened layer on the surface under abrasive wear conditions, effectively suppressing the propagation of microcracks and further enhancing the wear resistance of the cladding metals. However, excessive addition of Y_2O_3 causes the microstructure of the cladding metal to coarsen, thereby weakening its wear resistance.

Fig. 10 shows the wear morphologies of cladding metals with different Y_2O_3 contents. In the Y_2O_3-free sample, the worn surface exhibits deep plowing grooves accompanied by obvious plowing wrinkles, peeling pits, and visible surface cracks. The addition of 0.2wt% nano-Y_2O_3 to the cladding metals results in a reduction in the number of surface wrinkles and peeling pits, as well as the depth of plowing grooves. When the Y_2O_3 content increases to 0.4wt%, the wear marks on the surface of the cladding metals are minimized and uniformly distributed, with no peeling pits observed, indicating optimal wear resistance of the cladding metals. However, as the Y_2O_3 content continues to increase, the wear marks on the surface of the cladding metals deepens, and debris and plowing wrinkles appear, indicating deteriorated wear resistance. There are two mechanisms for the formation of debris: micro-cutting and local fracture peeling. The abundant plowing features indicate that the wear mechanism of the alloys is mainly abrasive wear. As shown in Table 4, region B consists of $M_{23}(C,B)_6$ eutectic carbides embedded in

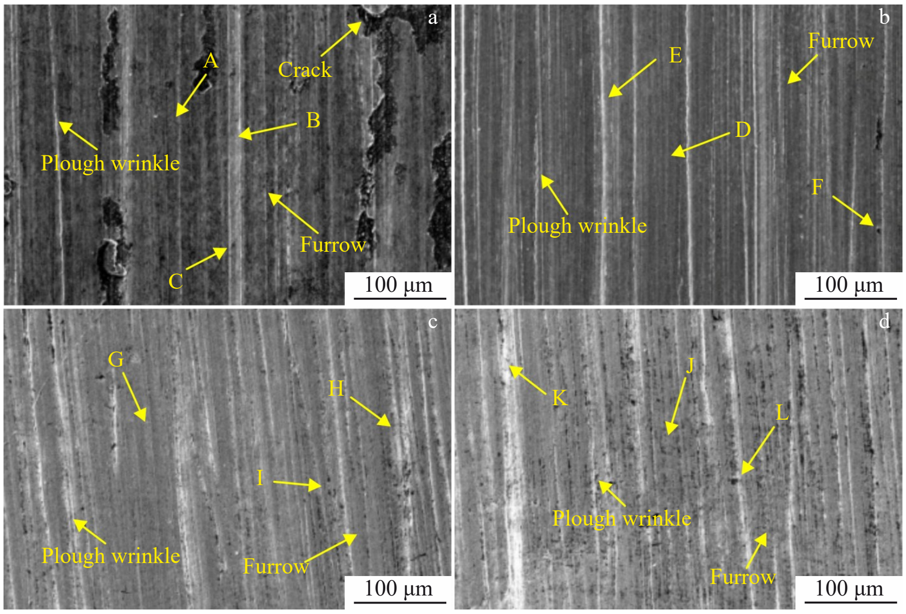

Fig.10 Wear morphologies of cladding metals with different Y_2O_3 contents: (a) 0wt%, (b) 0.2 wt% (c) 0.4wt%, and (d) 0.5wt%

Table 4 EDS analysis results of points marked in Fig.10 (wt%)

Point	B	C	Ti	Cr	Fe	Y
A	3.99	5.81	0.63	15.21	74.36	-
B	1.61	3.40	0.65	26.86	67.48	-
C	2.65	11.84	42.63	12.87	30.01	-
D	5.55	4.48	0.85	13.86	75.12	0.14
E	2.04	4.69	0.91	26.89	65.28	0.19
F	2.41	14.55	47.20	10.11	25.73	0.20
G	5.51	4.52	0.96	11.53	77.17	0.31
H	5.94	4.05	1.14	22.44	66.02	0.41
I	3.94	9.83	46.02	11.57	28.27	0.37
J	5.50	5.79	1.38	11.68	75.27	0.38
K	3.91	6.86	1.91	22.03	64.82	0.47
L	3.38	9.48	48.51	10.65	27.49	0.49

the γ-Fe matrix, acting as a wear-resistant skeleton due to their high hardness. Region C contains TiC particles, whose dispersed distribution hinders the movement of dislocations, thereby contributing to the wear resistance. The appropriate addition of Y_2O_3 can promote the precipitation of TiC hard phase and optimize the distribution of M_{23}(C, B)$_6$ eutectic carbide. These changes have a significant positive impact on the wear resistance of the cladding metals.

Fig.11 shows schematics of abrasive wear mechanism. The hard phases of cladding metals is mainly composed of TiC particles combined with M_{23}(C, B)$_6$ eutectic carbides. Among them, M_{23}(C, B)$_6$ eutectic carbides have high hardness and are uniformly embedded in the matrix in a regular grid shape, serving as a wear-resistant skeleton. In addition, a large amount of dispersed TiC hard phase particles also play a positive role in the overall wear resistance of the cladding metals. In the Y_2O_3-free cladding metals, the precipitation of TiC hard phase is relatively limited, restricting the effective display of wear resistance. On the contrary, when Y_2O_3 is appropriately introduced into the cladding metals, the precipitation of TiC hard phase significantly increases, the distribution of hard phase is more uniform, and the spacing between particles decreases. The dispersed TiC particles hinder the movement of dislocations, contributing to the wear resistance. This structure prevents abrasives from continuously cutting the substrate, effectively improving the wear resistance of the cladding metals.

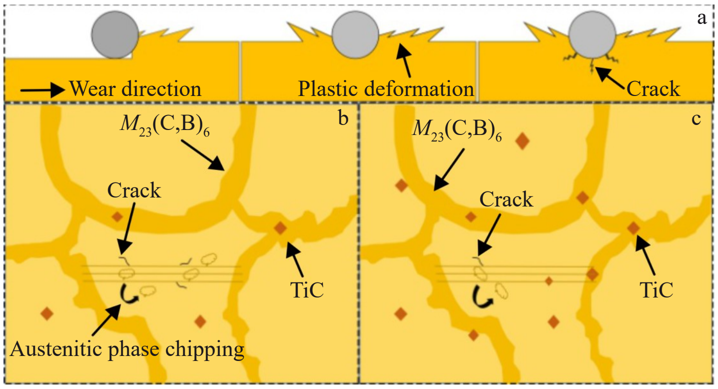

Fig.11 Schematics of abrasive wear mechanism: (a) different processes, (b) low TiC precipitation, and (c) high TiC precipitation

4 Conclusions

1) The appropriate addition of Y_2O_3 into Fe-Cr-C-B-Ti cladding metal can significantly improve the formability quality. Specifically, when the Y_2O_3 content reaches 0.4wt%, the cladding metal exhibits the optimal formability, with the wetting angle gradually decreasing to 52.2°.

2) There phase composition of the cladding metals remains unchanged with varying Y_2O_3 content. The microstructure in the cladding metals is still composed of austenite γ-Fe+ M_{23}(C,B)$_6$ eutectic carbide+TiC hard phase. When the content of Y_2O_3 is 0.4wt%, the precipitation of TiC hard phases and M_{23}(C,B)$_6$ eutectic carbides is maximized, accompanied by the finest microstructures.

3) Compared with the Y_2O_3-free cladding metals, the Y_2O_3-modified cladding metals exhibit significantly improved wear resistance and hardness. When the Y_2O_3 content reaches 0.4wt%, the hardness of the cladding metals increases sharply to 89.7 HRC, with an increment of 47%. At the same time, the wear mass loss is reduced to a minimum of 0.27 g, representing a 55.56% enhancement in wear resistance. The wear behavior of the cladding metals is dominated by abrasive wear, which involves micro-cutting and plowing mechanisms during the wear process.

4) The wear resistance of cladding metals is closely related to the size, quantity, and distribution of secondary phases. Future work may include a comprehensive analysis based on the present research findings. In addition, investigating the wear resistance of cladding metals with different welding passes can also be a promising direction.

References

1 Venkatesh B, Sriker K, Prabhakar V S V. *Procedia Materials Science*[J], 2015, 10: 527

2 Li J, Kannan R, Shi M H et al. *Metall Mater Trans B*[J], 2020, 5(8): 1291

3 Feldshtein E, Kardapolava M, Dyachenko O. *International Journal of Applied Mechanics and Engineering*[J], 2018,

23(2): 851
4 Debta M K, Masanta M. *International Journal of Refractory Metals and Hard Materials*[J], 2023, 7(16): 106078
5 Shi Z J, Liu S, Guo J B *et al. Journal of Materials Science*[J], 2019, 54: 10102
6 Zhang T G, Xiao H Q, Zhang Z Q *et al. Journal of Materials Engineering and Performance*[J], 2020, 29(12): 8221
7 Zhang K M, Zou J X, Jun L *et al. Transactions of Nonferrous Metals Society of China*[J], 2012, 22(8): 1817
8 Liu S, Shi Z J, Xing X L *et al. Materials Today Communications*[J], 2020, 5(24): 101232
9 Wang X H, Liu S S, Zhang M *et al. Tribology Transactions*[J], 2020, 63(2): 345
10 Liang X W, Su Y H, Yang T S *et al. JOM*[J], 2023, 6(8): 1
11 Ai X Y, Liu Z J, Zou Z X. *Crystals*[J], 2023, 13: 1023
12 Bramfit B L. *Metallurgical Transactions*[J], 1969, 1: 1978
13 Liu S, Zhang J, Wang Z J *et al. Materials Characterization*[J], 2017, 5(132): 41
14 Liu S, Wang Z J, Shi Z J *et al. Journal of Alloys and Compounds*[J], 2017, 691(1): 239
15 Debta M K, Masanta M. *International Journal of Refractory Metals and Hard Materials*[J], 2023, 7(164): 66
16 Lu D, Liu S, Zhang X *et al. Surface & Interface Analysis*[J], 2015, 47(2): 239
17 Su Y H, Liang X W, Liu Y Q *et al. Acta Metallurgica Sinica (English Letters)*[J], 2020, 33(7): 957
18 Wang M L, Cui H Z, Wei N *et al. ACS Applied Materials & Interfaces*[J], 2018, 10(4): 4250

Y含量对Fe-Cr-C-B-Ti熔覆金属成型性及磨损性能影响

郭建波，刘政军，苏允海
(沈阳工业大学 材料科学与工程学院，辽宁 沈阳 110870)

摘　要：磨损、腐蚀、疲劳构成了机械零件失效的3种形式，其中机械零件的磨损造成的能源消耗和经济损失尤为严重。通过等离子堆焊的方法制备Fe-Cr-C-B-Ti-Y系耐磨熔覆金属。采用MLS-23型橡胶轮式湿砂磨损试验机分析了熔覆金属的磨损性能。采用XRD、SEM、EBSD和TEM分析了熔覆金属的物相组成和显微组织，并对合金的强化机理和磨损机理进行了探讨。结果表明：Fe-Cr-C-B-Ti-Y熔覆金属中显微组织由奥氏体γ-Fe+M_{23}(C,B)$_6$共晶碳化物+TiC硬质相组成。随着Y_2O_3添加量的增多，熔覆金属的硬度与磨损量呈现先增加后减小的变化趋势。当Y_2O_3含量为0.4wt%时，TiC硬质相与M_{23}(C,B)$_6$共晶碳化物析出量最多，组织晶粒最为细小。熔覆金属成型性最好，润湿角最小，为52.2°。此时，熔覆金属的洛氏硬度值为89.7 HRC，磨损失重为0.27 g。熔覆金属的磨损机制主要为磨粒磨损，材料的去除过程为显微切削与犁沟。

关键词：Fe-Cr-C-B；熔覆金属；纳米Y_2O_3；陶瓷相；耐磨性

作者简介：郭建波，男，1980年生，博士生，沈阳工业大学材料科学与工程学院，辽宁 沈阳 110870，E-mail： GUOJIANBO@126.com